PAPER

Check for updates

Tuning of structural and optical properties with enhanced catalytic activity in chemically synthesized Co-doped MoS$_2$ nanosheets†

Rosy Rahman,[a] Dipanjan Samanta,[b] Amita Pathak*[b] and Tapan Kumar Nath [ID] *[a]

Molybdenum disulfide (MoS$_2$) nanosheets, due to having a highly active nature, being low cost and having unique physical and chemical properties, have shown their efficacy in the catalytic reduction of nitroarenes. Doping of transition metal ions in molybdenum disulfide (MoS$_2$) nanosheets is a well-known strategy to enhance their catalytic efficiency for the reduction of nitroarenes, however, finding the optimum dopant amount is still a subject of ongoing research. Herein, we have synthesized few-layered cobalt (Co) doped MoS$_2$ nanosheets with different cobalt content (2%, 4%, 6% and 8%) through the solvothermal approach, taking sodium molybdate dihydrate (Na$_2$MoO$_4$·2H$_2$O), thiourea (CH$_4$N$_2$S) and cobalt acetate tetrahydrate [Co(CH$_3$COO)$_2$·4H$_2$O] as precursors and their catalytic performance has been affirmed by monitoring the reduction of *p*-nitrophenol by NaBH$_4$ in real time using UV-visible absorption spectroscopy. The 6% Co doped MoS$_2$ nanosheets have exhibited superior catalytic activity with a pseudo-first order rate constant of 3.03×10^{-3} s^{-1} attributed to the abundant defects in the active edge sites having a dominant metallic 1T phase with Co ion activated defective basal planes, sulphur (S) edges, synergistic structural and electronic modulation between MoS$_2$ and Co ions and enhanced electron transfer assisted through redox cycling in the active sites. An attempt has also been made to study the manipulation of structural and optical properties with cobalt doping in MoS$_2$ nanosheets to establish a correlation between the catalytic efficiency and dopant content. This study demonstrates that proper tuning of Co doping in MoS$_2$ nanosheets paves the way in searching for a potential alternative of a noble metal catalyst for the catalytic reduction of nitroarenes.

1. Introduction

Graphene-like two-dimensional (2D) transition metal dichalcogenides[1] (TMDs) have garnered a lot of interest because of their fascinating structural and electronic properties which make them suitable as catalysts in various technologically important applications such as electrochemical generation of hydrogen from water[2–4] and hydro-desulfurization of petroleum.[5,6] One of the most widely studied TMD systems includes layered MoS$_2$. It is commonly known to exist in two crystallographic forms: (i) the thermodynamically stable trigonal prismatic (2H) phase (space group $P6_3/mmc$)[7] and (ii) the metastable octahedral (1T) phase (space group $P3m1$).[8] Among these 1T MoS$_2$ is reported to show metallic behaviour[9] whereas the 2H MoS$_2$ is an indirect semiconductor having a band gap of ~1.2 eV.[10] The electronic properties of 2H MoS$_2$ can be tailored by changing the layer thickness,[10] doping of TM metal ions[11] and introducing tensile lattice strain.[12] Theoretical and experimental studies indicate that the catalytic activity of thermodynamically stable 2H polymorph of MoS$_2$ is associated with its metallic edges, whereas its semiconducting basal plane is proved to be catalytically inert.[2,4]

p-Nitrophenol (*p*-NP) is one of the most common and stubborn harmful organic pollutants found in industrial wastewaters. However, its reductive derivative, *p*-aminophenol (*p*-AP) is widely used in manufacturing of drugs such as paracetamol and clofibrate and also used as a developing agent in photography and as a petroleum additives.[13–15] Therefore, the catalytic transformation of *p*-NP into *p*-AP has been extensively studied as a model reaction to verify the activity of a catalyst during the past few years.[16–18] Most of these studies were focused on the activity of noble-metal nanoparticles (NPs) such as Ag, Au, Pd and Pt. Although they possess high catalytic potential, however, their usage may lead to depletion of rare resources, environmental contamination and health issues. In addition, the agglomeration of colloidal noble metal NPs during the catalytic reaction is often inevitable.

In this regard, MoS$_2$, a 2D layered material, acts as an efficient candidate in catalytic reduction of *p*-NP as its basal plane

[a]Department of Physics, Indian Institute of Technology Kharagpur, W. B., 721302, India. E-mail: tnath@phy.iitkgp.ac.in; tapnath@gmail.com

[b]Department of Chemistry, Indian Institute of Technology Kharagpur, W. B., 721302, India

and catalytic edges with increased exposed active sites facilitate the electron transfer process.[19] Recently, various nanostructures of MoS$_2$, amorphous[20–22]/crystalline[23–26] and vertically aligned structures[27,28] have been explored to maximize the number of active edge sites. Hybridization of MoS$_2$ with conducting/semiconducting/magnetic materials (graphene[28–32]/CoSe$_2$ (ref. 33)/CoS[34–37]/CdS[38,39]/Fe$_3$O$_4$ (ref. 40)) is able to enhance the catalytic activity through synergistic coupling effects. Metastable, intrinsically metallic, octahedral 1T MoS$_2$ obtained through exfoliation of trigonal prismatic 2H MoS$_2$ has proven to be an excellent catalyst for H$_2$ evolution reactions. The 1T phase facilitates electrode kinetics by increasing the electrical conductivity and proliferation of the catalytic active sites.[41–43] Noble metal (Au, Ag, Pd, Pt)-MoS$_2$ nanocomposite has proven to be as efficient catalyst, although such type of synthesis procedure includes controlled reaction condition, stabilizing agent and high cost.[44] Introducing transition metal ions (Co, Ni, Fe) into the MoS$_2$ matrix has been the classic route to maximize the catalytic activity of MoS$_2$ as the doped ions alter the electronic properties at the coordinatively unsaturated catalytic S-edges.[23,45,46] These strategies have been designed largely to either optimize the density of active edge sites by reducing the dimensions along the z direction or xy direction (nanostructures)[47] or increase the conductivity by stabilizing the 1T MoS$_2$ polytype.[32,41,42]

Introduction of cobalt ion in 2H MoS$_2$ may be a fascinating strategy in doping as it can increase the types and numbers of active sites in the basal planes in addition to edges[48,49] along with introduction of 1T phase in 2H phase. It also exhibits ready redox Co^{2+} ↔ Co^{3+} switching and can alter the band positions favourably. Intrinsic defects in the form of Mo vacancies and sulphur vacancies as well as extrinsic donor and acceptor defects resulting from doping are used to improve the semiconducting properties generally through band gap reduction by lowering the conduction band, raising the valence band, and/or introducing midgap states. These defects can act as electron and hole traps, which can increase the recombination times and alter the recombination rates resulting enhancement in catalytic efficiency than the pristine one.

One of the standard reactions to test the catalytic action is the reduction of p-NP by NaBH$_4$. Nitrophenol, with aromatic rings associated with H-bonding –NO$_2$ and –OH groups, enables the reduction to be carried out in water making it an environment-friendly reaction. In this work we have investigated in detail the tuning with Co doping on structural, optical properties and catalytic activity in chemically synthesized MoS$_2$ nanosheets having the mixture of both 1T and 2H phases. Attempt has also been made to establish a correlation between its observed optical properties with the catalytic efficiency as the doping concentration of Co is increased in MoS$_2$ nanosheets. This study demonstrates that catalytic efficiency of MoS$_2$ nanosheets can be enhanced with increased amount of cobalt doping percentages (2 at. wt%, 4 at. wt%, 6 at. wt%). As Co-doping percentage is increased in MoS$_2$ nanosheets, the band gap is reduced along with increased active sites which facilitate electron transfer easily resulting exceptional catalytic activity in the reduction of nitrophenol to aminophenol. The observed

turnover frequency (TOF) in Co–MoS$_2$ (6 at. wt%) is far superior in comparison with other MoS$_2$ architectures and noble-metal-based catalysts, graphene based nanocomposites *etc.* reported so far.

2. Experimental details

2.1. Chemicals used

High purity (99.9% purity) chemicals, like sodium molybdate dihydrate (Na$_2$MoO$_4$·2H$_2$O), thiourea (CH$_4$N$_2$S), sodium borohydride (NaBH$_4$), acetic acid (CH$_3$COOH), p-nitrophenol (C$_6$H$_5$NO$_3$), cobalt acetate tetrahydrate (CO(CH$_3$COO)$_2$·4H$_2$O), ethyl alcohol (CH$_3$CH$_2$OH) were procured from Sigma-Aldrich. All the reagents are analytical reagent grade and used without further purification.

2.2. Synthesis of ultra-thin MoS$_2$ nanosheets

Pure and Co doped MoS$_2$ nanoparticles/nanosheets were synthesized in aqueous solution using sodium molybdate dihydrate (Na$_2$MoO$_4$·2H$_2$O), thiourea (CH$_4$N$_2$S) *via* simple hydrothermal technique in the starting solution mixture. In a typical synthesis, 2 mM of Na$_2$MoO$_4$·2H$_2$O and 5 mM of CH$_4$N$_2$S were dissolved in 40 mL of deionized water and were stirred for 30 minutes to obtain the clear starting solution mixture. The pH of the solution mixture was maintained at 5.0 by adding 0.02 mol L^{-1} of acetic acid (CH$_3$COOH) solution under stirring. This solution mixture was then transferred to a 50 mL Teflon lined stainless steel autoclave and was subjected to hydrothermal treatment at 200 °C for 24 hours under autogenous pressure. The autoclave was then allowed to cool naturally and the obtained black precipitate was separated through centrifugation for 30 minutes. Then the precipitate was washed thoroughly with ethanol and water several times for removal of surface adsorbed ions and impurities. The final product was dried in oven at 80 °C overnight and used for further characterization.

2.3. Synthesis of cobalt (2 at. wt%, 4 at. wt%, 6 at. wt% and 8 at. wt%) doped MoS$_2$ NSs

For the synthesis of 2 at. wt%, 4 at. wt%, 6 at. wt% and 8 at. wt% Co-doped MoS$_2$ samples, appropriate amount of cobalt acetate tetrahydrate [Co(CH$_3$COO)$_2$·4H$_2$O] aqueous solution was added to the former starting solution mixture and stirred very well prior to hydrothermal treatment at 200 °C for 24 hours. The rest of the procedure of separation, purification and collection of the dried as-synthesized samples was repeated as before (Fig. 1).

2.4. Characterization of nanostructures

The crystalline phase of respective as-synthesized undoped and Co doped MoS$_2$ samples were ascertained through powder X-ray diffraction (XRD) studies. It was carried out employing a Bruker AXS diffractometer D8, Germany using CuK$_\alpha$ radiation (λ = 1.5418 Å) at an applied voltage of 40 kV and at a scan rate of 3° min^{-1} in the 2θ range of 10°–70°. The presence of surface functional groups in the synthesized MoS$_2$ samples were established through Fourier-transformed infrared (FTIR)
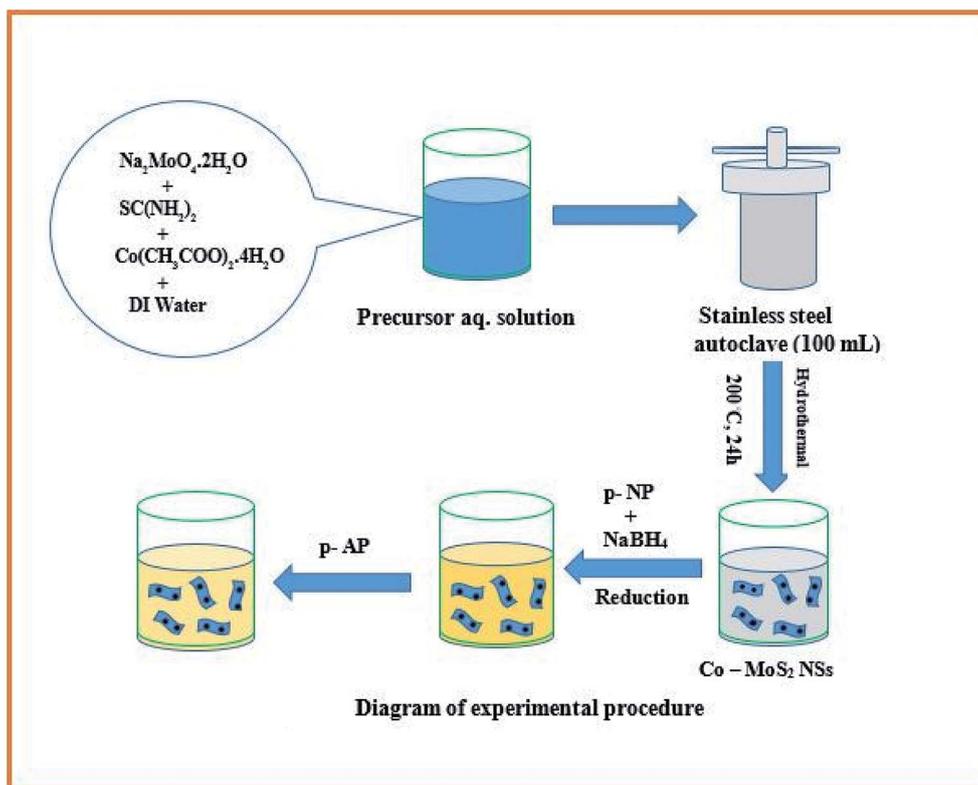
Fig. 1 Diagram of experimental procedure.

spectroscopy carried out between 4000 to 400 cm^{-1} using a Perkin–Elmer Spectrum RX-II Model 73713, USA. The microstructural features of the synthesized MoS$_2$ samples were analyzed by transmission electron microscopy (TEM, FEI-TECNAI G2 20S-TWIN, USA) imaging and high-resolution transmission electron microscopy (HRTEM, JEOL JEM-2100, Japan) imaging at an acceleration voltage of 200 kV. Zeta potential measurement was undertaken to determine the surface charge of the samples using a Malvern Nano ZS

instrument. The optical and catalytic activity of the samples was investigated through a Shimadzu-2450 UV-vis-NIR spectrophotometer, Japan. The band gap energies of the samples were evaluated from UV-vis absorption spectra using the Tauc plot. Scanning electron microscopy (SEM) analysis was carried out using a Zeiss, Ultra 55 field emission scanning electron microscope equipped with energy-dispersive X-ray spectroscopy (EDS). The Raman spectra of the samples were recorded on HORIBA Jobin-YvonLabRAM HR800 at 532 nm excitation wavelength.
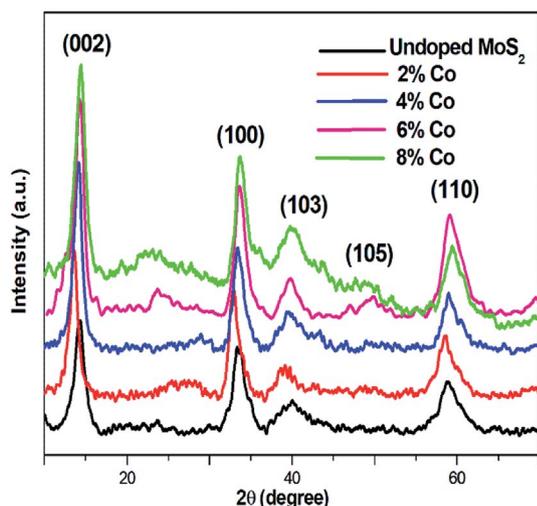
3. Results and discussion

3.1. Structural study (XRD data analysis)

The room temperature HRXRD (Fig. 2) patterns of undoped and the Co-doped MoS$_2$ nanostructures of different doping concentration were recorded over 2θ range of 10°–70° to verify the formation of crystalline phases of MoS$_2$. The HRXRD data

Fig. 2 XRD pattern of undoped and Co doped MoS$_2$.

Table 1 The microstructural parameters of the undoped and Co doped MoS$_2$ nanostructures

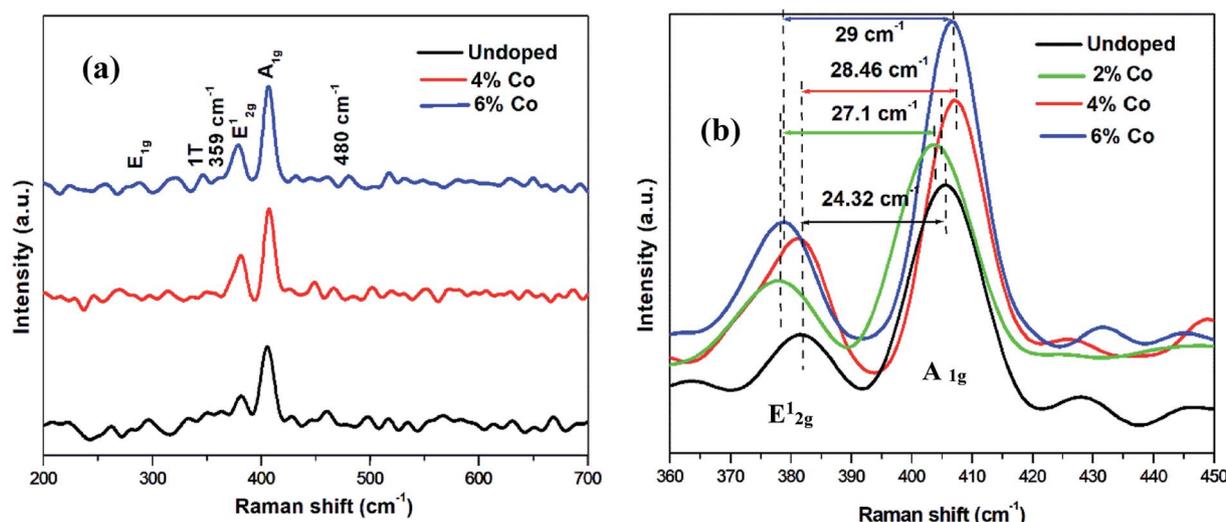| Co doping percentages	Crystallite size (nm)	Microstrain ε	Dislocation density δ (lines per m^2)
0%	8.11	3.98×10^{-3}	1.52×10^{16}
8%	7.44	5.17×10^{-3}	1.81×10^{16}

Fig. 3 (a) Raman spectra for undoped and Co doped MoS$_2$ (b) zoomed view.

reveals that 2H MoS$_2$ phase is formed having diffraction peaks at 14.2°, 33.4°, 39.7°, 49.7°, 58.8° (PDF 65-1951). It is clearly seen that the crystalline quality is improved with doping of maximum percentages of cobalt. The broadening of peaks has been observed with increase of Co doping concentration due to appearance of lattice strain. Since the ionic radius of Co^{2+} (0.074 nm) is slightly larger than that of Mo^{4+} (0.065 nm), it is expected to develop a lattice strain. The crystallite sizes of the MoS$_2$ nanostructures were estimated by Scherrer formula.

$$D_{hkl} = k\lambda/(\beta_{hkl} \cos \theta)$$

Here, k is a coefficient ($k = 0.9$), β is the full width at half maximum of the (002) peak, and λ is the incident X-ray wavelength ($\lambda = 0.154$ nm). The crystallite sizes D of the undoped and the 8% Co doped MoS$_2$ samples are estimated to be 8.11 nm and 7.44 nm, respectively. The microstrain (ε) and dislocation density (δ) appearing in the lattice due to some substitution of Mo atoms by Co atoms can be calculated from the following relations:

$$\varepsilon = \beta \cos \theta/4, \ \delta = 1/D^2$$

The values of crystallite size, microstrain and dislocation density are calculated and summarized in Table 1.

3.2. Raman spectroscopy study

The recorded Raman spectra of MoS$_2$ and Co doped MoS$_2$ are shown in Fig. 3(a). The characteristic peaks at 282, 380, 406 and 458 cm^{-1} correspond to the E$_{1g}$, E$^1_{2g}$, A$_{1g}$, and A$_{2u}$ phonon modes of 2H-MoS$_2$. The peak arising due to 1 T-phase of MoS$_2$ is identified at 345 cm^{-1} (ref. 50) suggesting that the as-synthesized flower-like MoS$_2$ consists of mixed 2H and 1T phases. 18% incorporation of 1T phase in undoped sample and 73% incorporation of 1T phase in 6% Co doped MoS$_2$ samples were obtained. In addition to these peaks, two new peaks emerge at 359 cm^{-1} and 480 cm^{-1} for Co^{2+} doped MoS$_2$ nanostructures. Furthermore, the peak intensity is generally higher with higher doping concentration.[51] This suggests that these peaks may belong to the local vibrational modes associated with the Co^{2+} dopants.

It is clearly observed that with increase in cobalt doping, E$^1_{2g}$ vibration mode is decreased, while the A$_{1g}$ vibration mode is increased, which are related to the tensile strain[52] appearing in the lattice due to doping of cobalt ion in Mo site and number of layer in MoS$_2$.[53] When the layer number increases, the interlayer van der Waals force in MoS$_2$ suppresses atomic vibration, resulting in higher force constants resulting in stiffening of A$_{1g}$ mode (blue-shift). On the contrary, E$^1_{2g}$ peak shows a red-shift, instead of a blue-shift, suggesting that the increased interlayer van der Waals force plays a minor role while stacking-induced structure changes or long-range coulombic interlayer interactions in multilayer MoS$_2$ may dominate the change of atomic vibration.[54] Additionally, the intensity ratio of A$_{1g}$ to E$^1_{2g}$ mode is 2.17 which concludes that it favours the vibration of A$_{1g}$ mode and thus the best edge-terminated structure.[55] According to the dependence of A$_{1g}$ full width at half maximum (FWHM) on the MoS$_2$ thickness, this decrease in FWHM in 6% Co doped MoS$_2$ is an indication of thinning down the effective MoS$_2$ thickness.[50] The positions of the characteristic Raman E$^1_{2g}$ and A$_{1g}$ peaks and their separations with varying cobalt doping concentrations are summarized in Table 2.

Table 2 Comparison of characteristic Raman peak position with varying doping concentration of cobalt ions in MoS$_2$

Co doping percentages	E$^1_{2g}$ (cm^{-1})	A$_{1g}$ (cm^{-1})	Δk (cm^{-1})
0%	381.45	405.77	24.32
2%	379.49	406.59	27.10
4%	378.63	407.09	28.46
6%	378.23	407.23	29.00

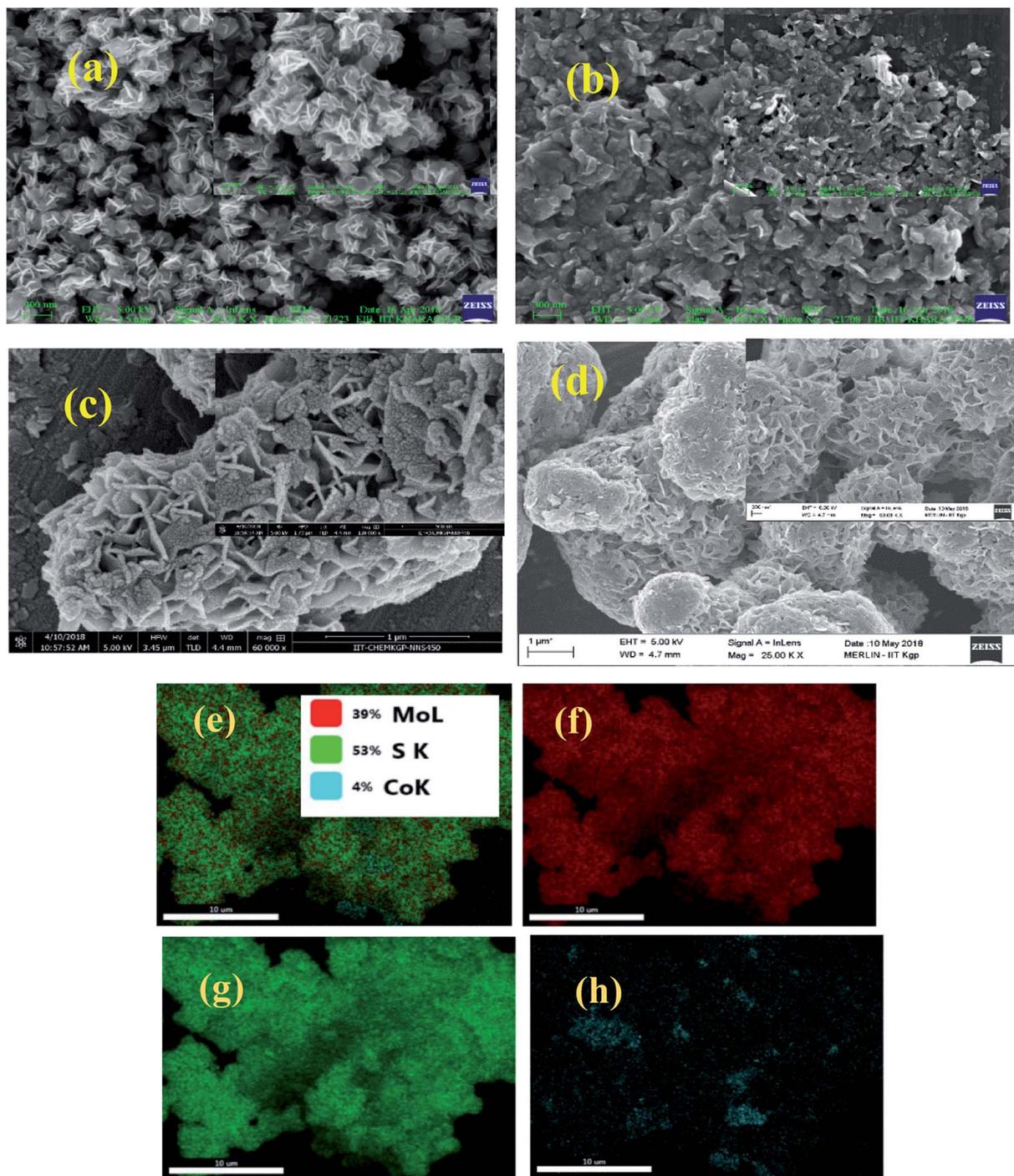© 2021 The Author(s). Published by the Royal Society of Chemistry

Fig. 4   SEM images of (a) undoped (b) 2% Co, (c) 4% Co and (d) 6% Co doped MoS$_2$ nanostructures (e) EDS elemental mapping of Mo, S and Co components for 4% Co doped MoS$_2$ (f) Mo, (g) S, (h) Co EDAX mapping for 4% Co doped MoS$_2$.

3.3.   Morphology and microstructure

SEM image analysis. The observed surface morphology of the as-prepared samples was analyzed based on recorded SEM and TEM images. As shown in Fig. 4(a), the pristine MoS$_2$ exhibits dispersed nanosheet like morphology. Fig. (b)–(d) show the nanostructures of 2%, 4% and 6% Co doped MoS$_2$ samples. With the incorporation of dopant ion, the dispersed flakes are interlaced by rolling up of surface edges. They form nano-flowers by summing up of nano-flakes (thickness within 10 nm). From EDX analysis of 4% cobalt doped MoS$_2$ it can be seen that S : Mo atomic ratio is 1.4 : 1. It indicates that some oxygen vacancies are created along with doping. It also shows accurate detection of the amount of cobalt doped in the sample.

HRTEM image analysis. Fig. 5 shows detailed microstructure of the MoS$_2$ nanosheet samples recorded by using HRTEM
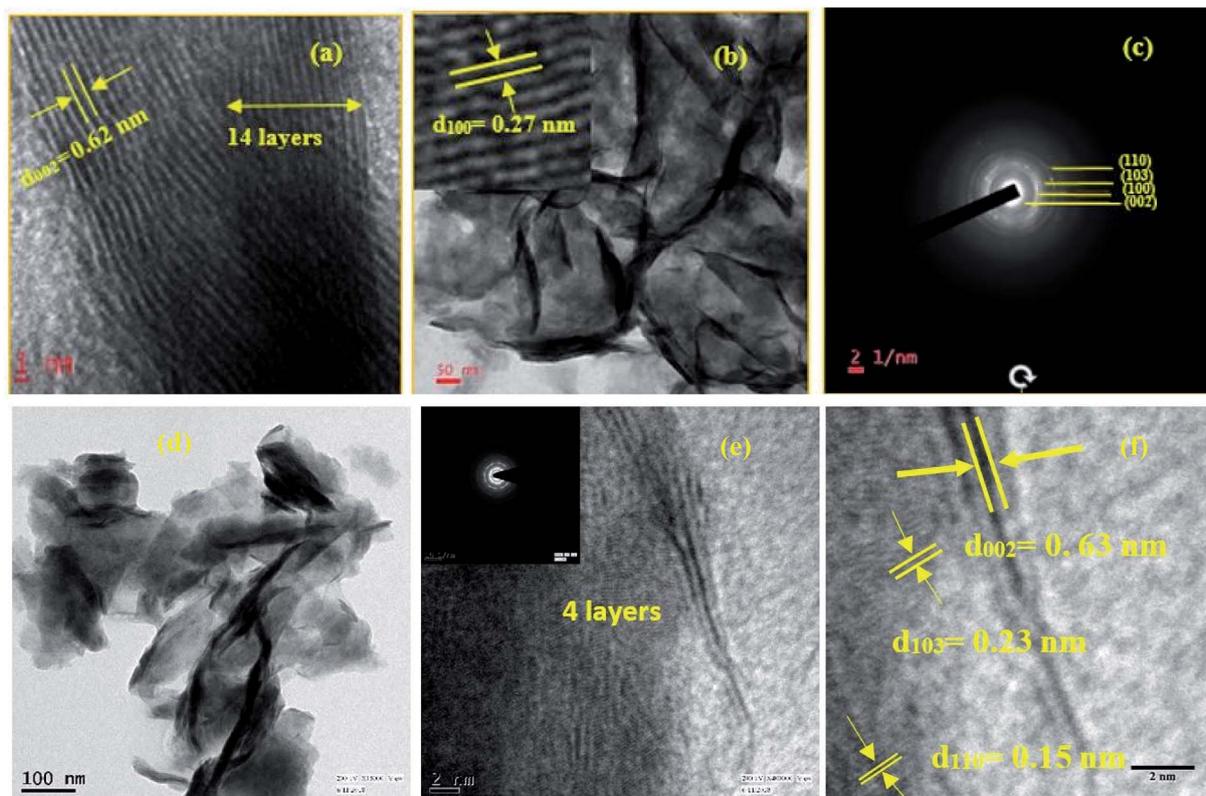
Fig. 5 HRTEM images (a) showing layer numbers and interlayer separation between (002) planes (b) interlaced flake size having lateral dimension ~40 nm and (100) interplanar spacing (inset) 0.27 nm (c) SAED pattern for different orientation of planes for undoped MoS_2; (d) interlaced nanoflakes with lateral dimension ~20 nm, (e) layer distribution and SAED pattern (inset) and (f) lattice fringes and interlayer separation between (002) planes for 6% Co^{2+} doped MoS_2 samples.

imaging. Fig. 5(a) clearly shows the magnified image of interlaced flakes of undoped MoS_2 where interlayer distance is found to be 0.62 nm forming a 14 layer system. Inset of Fig. 5(b) shows the interplanar distance between (100) planes and it is found to be 0.27 nm, which matches very well with SAED ring pattern corresponding to (100) plane as shown in Fig. 5(c). The undoped MoS_2 reveals polycrystalline nature which is clear from SAED

pattern and four distinct rings appears corresponding to planes (002), (100), (103) and (110) which are also seen in XRD pattern. Similar results can also be obtained from Fig. 5(f) of 6% Co doped MoS_2. Lattice spacing for (002), (110), (103) planes are 0.63 nm, 0.15 nm and 0.23 nm, respectively. It exactly matches with results obtained from SAED pattern in Fig. 5(e) (inset). Again (004) plane is prominent in 6% Co doped MoS_2 sample
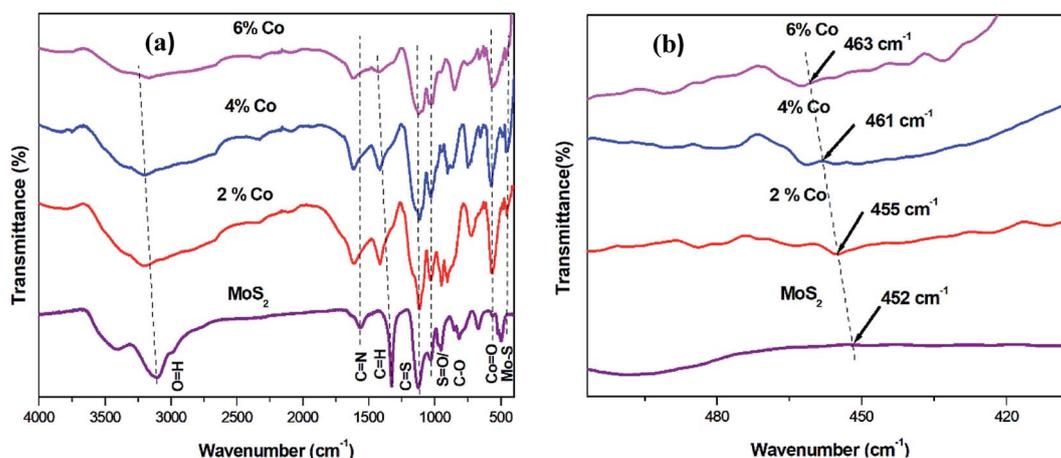

Fig. 6 (a) FTIR spectra for undoped and Co doped MoS_2 (b) zoomed view of shifting of Mo–S peak.

Fig. 7 XPS narrow scan spectra of Mo 3d (a) and (d) and S 2p (b) and (e), for undoped, 6% Co doped MoS$_2$, narrow scan spectra of Co 2p (g) of 6% Co doped MoS$_2$. Survey spectra of Mo (3d, 3p, 3s), S 2p, C 1s, Co 2p (c), (f) for undoped and 6% Co doped MoS$_2$.

which is a layered material as confirmed from our SEM and TEM results. By comparing Fig. 5(b) and (e) of microstructures corresponding to undoped and 6% Co doped MoS$_2$ we can ascertain that the multi-layered nanoflakes in undoped MoS$_2$ are exfoliated and thinned down to few layers in 6% Co doped MoS$_2$ due to cobalt ion intercalation in the basal plane of the layered structure. This is also consistent with AFM image analysis (ESI, Fig. S1†).

3.4. FTIR data analysis

FTIR measurements were carried out in order to obtain the bending and stretching vibrations of functional groups present in the undoped and Co doped MoS$_2$ samples. Fig. 6 depicts the FTIR spectra of all the samples under investigations. The weak peak observed at about 452 cm^{-1} is assigned to Mo–S vibration in undoped MoS$_2$. The peak corresponding to 1035 cm^{-1} is

Table 3 Variation of oxidation peaks of Mo, S and Co in MoS$_2$ with cobalt doping

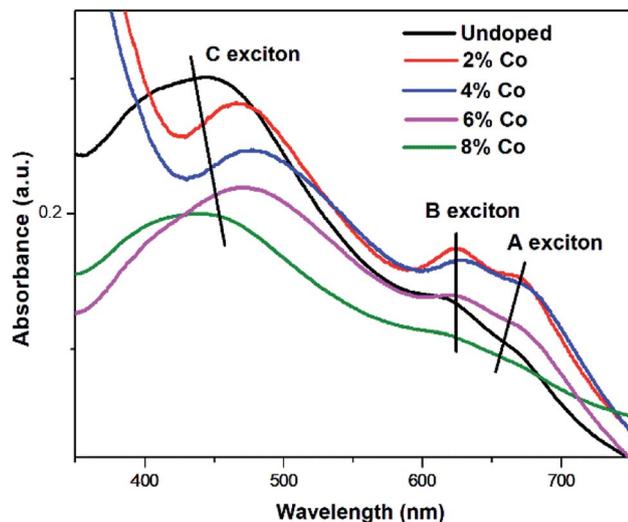|	1T		2H		1T		2H		Co^{3+}		Co^{2+}		
Doping%	Mo 3d$_{5/2}$ (eV)	Mo 3d$_{3/2}$ (eV)	Mo 3d$_{5/2}$ (eV)	Mo 3d$_{3/2}$ (eV)	S 2p$_{3/2}$ (eV)	S 2p$_{1/2}$ (eV)	S 2p$_{3/2}$ (eV)	S 2p$_{1/2}$ (eV)	Co 2p$_{3/2}$ (eV)	Co 2p$_{1/2}$ (eV)	Co 2p$_{3/2}$ (eV)	Co 2p$_{1/2}$ (eV)	O 1s (eV)
0%	228.25	231.12	229	231.5	161.78	162.03	162.96	163.37	—	—	—	—	530.78
6%	228.62	231.75	229	232	161.48	162.75	162.07	163.57	779.25	794.75	781.25	797.75	530.88

Fig. 8 UV-vis absorption spectroscopy for undoped and Co doped MoS_2.

probably due to S–O (sulfoxide) asymmetric stretching or C–O bondstretching (alcohol group). The peaks around 1200 and 1628 cm^{-1} in the FTIR spectra of undoped MoS_2 and Co doped MoS_2 confirm the existence of C–S and C–N bonds, respectively. Moreover, a broad absorption band at about 3134 cm^{-1} appears in the FTIR spectra is assigned to stretching vibration of the O–H bond corresponding to intercalated water. The peak around 1400 cm^{-1} is probably due to C–H bending mode. In addition, the new peaks arising at 561 cm^{-1}, 567 cm^{-1} and 573 cm^{-1} for 2%, 4% and 6% Co doped MoS_2, respectively corresponding to Co–O stretching mode in tetrahedral site and octahedral environment. The peak corresponding to Mo–S vibration at 452 cm^{-1} for undoped MoS_2 shifts to 455 cm^{-1} for 2% Co, 461 cm^{-1} for 4% Co and 463 cm^{-1} for 6% Co doped MoS_2, respectively as shown in Fig. 6(b). Here the red shift of wave number indicates Co substitution in Mo site causing

decrease in effective mass of the whole system, oxygen vacancies and structural defects.[56,57]

3.5. Zeta potential measurement

The surface charges of undoped and Co doped MoS_2 were determined from zeta potential measurement using the aqueous dispersion in neutral condition (pH-7). High value of the zeta potential (either + or −) is indicative of the stability of particles against aggregation or flocculation in the dispersion medium. All four samples showed negative surface charge, may be due to presence of carboxyl group (–COOH) which has been added during synthesis. The zeta potential values for undoped, 2%, 4%, and 6% Co doped MoS_2 showed −48.3 mV, −41.2 mV, −37.5 mV and −30.8 mV, respectively.

3.6. XPS study

X-ray photoelectron spectroscopic (XPS) measurements were carried out to investigate the chemical composition of undoped and 6% Co doped MoS_2. As shown in the survey spectrum (wide scan) in Fig. 7(c) and (f), the elements C, Mo, S, and O can be clearly identified in undoped and C, Mo, S, O and Co in 6% Co doped MoS_2 nanosheets. The typical Mo $3d_{5/2}$ and Mo $3d_{3/2}$ peaks of 2H phase appeared at 229, 231.5 eV in undoped and 229, 232 eV binding energies in 6% Co doped MoS_2 along with two additional peaks shifted by about 1 eV which were assigned to Mo $3d_{5/2}$ and $3d_{3/2}$ of the 1T phase characteristic of the trigonal prismatic environment in 2H phase[58] as shown in Fig. 7(a) and (d). Similarly, the S $2p_{3/2}$ and S $2p_{1/2}$ peaks of 2H phase appeared at 162.96, 163.37 eV in undoped and 162.07, 163.57 eV in 6% Co doped MoS_2 binding energies, respectively as shown in Fig. 7(b) and (e). Two additional peaks shifted by about 1 eV (161.78, 162.03 eV (undoped), 161.48, 162.75 eV (6% Co doped)), from the S $2p_{3/2}$ and S $2p_{1/2}$ in 2H phase, were exhibited in both samples as expected for 1T sites. The peaks of Mo $3d_{5/2}$ and Mo $3d_{3/2}$ are shifted to higher binding energy with gradually increasing Co doping as observed in 6% Co doped MoS_2. The ratios of Mo^{5+} to Mo^{4+} for undoped, 2%, 4% and 6%
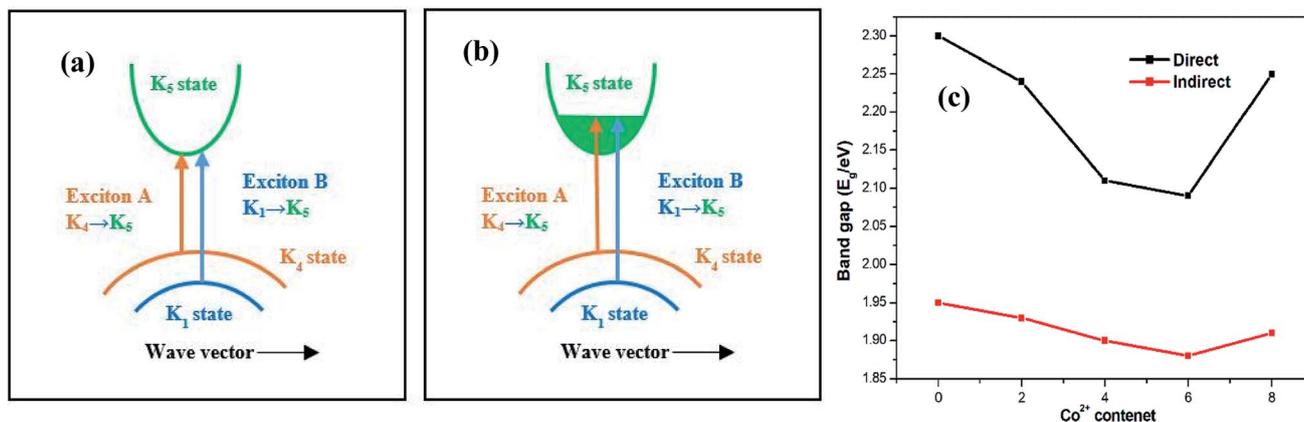

Fig. 9 Schematic view of the transitions corresponding to excitons A ($K_4 \rightarrow K_5$) and B ($K_1 \rightarrow K_5$) in (a) in 2H MoS_2 and (b) Burstein–Moss (BM) band-filling effect in heavy cobalt ion doping. Labels are according to ref. 64. (c) Variation of direct and indirect band gap with doping concentration.
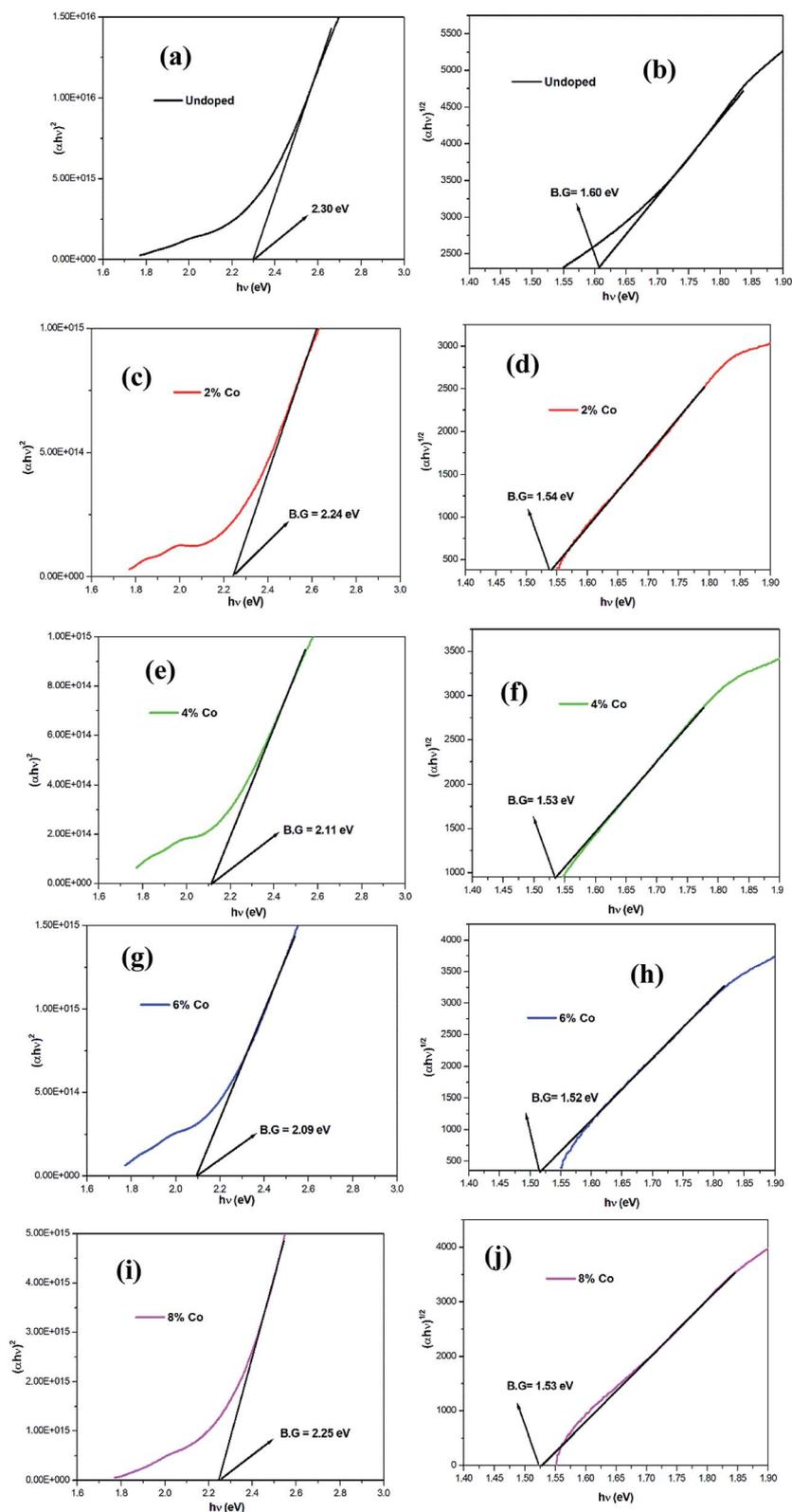
Fig. 10 Individual Tauc's plot for direct band gap (a), (c), (e), (g), (i) and indirect band gap (b), (d), (f), (h), (j) of undoped, 2%, 4%, 6% and 8% Co doped MoS_2.

Co doped MoS_2 are 0.28 : 1, 0.34 : 1, 0.63 : 1 and 0.71 : 1, respectively indicating the increased proportion of Mo^{5+} with increase of cobalt ion dopant. The separation of binding energy

between Mo $3d_{3/2}$ and $3d_{5/2}$ is 3.13 eV (1T phase) and 3 eV (2H phase) in 6% Co doped MoS_2, can be attributed to the dominant presence of Mo^{5+} ions in the cobalt doped samples[59] by redox

reaction of $Mo^{4+} \leftrightarrow Mo^{5+}$ supporting the earlier result. There are four main peaks corresponding to Co $2p_{3/2}$ at 779.25 eV (Co^{3+}), 781.25 eV (Co^{2+}) and Co $2p_{1/2}$ at 794.75 eV (Co^{3+}), 797.75 eV (Co^{2+}) in 6% Co doped MoS_2 as shown in Fig. 7(g). These peaks are very close to the binding energies of the Co species in CoS_2.[60-63] Also, another four peaks arising at 784.77, 787.75, 800.25, 802.62 eV signifies the presence of satellite shake up peaks. The binding energy of 779.25 eV is closed to what has been observed for $CoMo_2S_4$, suggesting that Co^{2+} substitutes Mo atoms along the {002} or the S-edge planes of MoS_2 indicating the uniform doping of cobalt ions in the MoS_2 substrate.[48] As cobalt doping percentages is increased, so a greater number of cobalt ions are substituting the Mo lattice site. All the binding energies, peak positions corresponding to Mo, S, Co and O in case of undoped and 6% Co doped MoS_2 are summarized in Table 3. The Mo 3d, S 2p and Co 2p spectrum with de-convoluted peaks of 2% and 4% Co doped MoS_2 nanosheets are shown in Fig. S3(a), (d), (b), (e), (c) and (f) respectively.† The presence of higher valence state of cations Mo^{5+} and oxygen existing in the doped sample suggests the probability of having partially oxidized Mo_2O_5 species in the doped sample which could result in the generation of oxygen vacancies in the sample. The binding energy of O 1s peaks found in both the species of MoS_2 centred at 530.78 eV (O (I)) belongs to the O^{2-} ions in the hexagonal structure of undoped MoS_2. The peaks centred at 530.88 eV (O (II)) belong to the oxygen vacancy defects in 6% Co and they can also serves as active sites for catalysis. In addition to redox couple present in the MoS_2 matrix, a third charge compensation mechanism is possible for matrix and dopant ions through intervalence charge transfer (IVCT).

$$Mo^{4+} + Co^{3+} \leftrightarrow Mo^{5+} + Co^{2+}$$
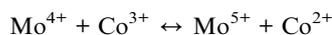
The XPS data presented here subsequently confirm that the precursor valence of Mo^{4+} and Co^{3+} partially alter to Mo^{5+} and Co^{2+}, which supports this mechanism.

3.7. Optical property study

UV-vis absorption spectroscopy and Tauc's plot. Fig. 8 shows the UV-visible absorption spectra of the undoped and different percentages of cobalt doped MoS_2 dispersed in DMF (dimethyl formamide). As expected, three typical characteristic absorption peaks of undoped and Co doped MoS_2 are clearly observed. A prominent peak centred in the region of 430–470 nm (C exciton), and two additional peaks with relatively lower intensity are observed around ~615 nm (B exciton) and ~670 nm (A exciton) which correspond to excitonic transitions between the split valence band and the minima of the conduction band at the K point of Brillouin zone for MoS_2 nanosheets.[64] The band gaps E_g (in eV) for undoped and cobalt doped MoS_2 nanostructures were calculated using the Tauc equation,

$$(\alpha h\nu)^{1/n} = B(h\nu - E_g)$$

where α is the absorption coefficient (in cm^{-1}), $h\nu$ is the incident photon energy (in eV), B is a constant relative to the materials, and $n = \frac{1}{2}$ (for direct allowed transition) and $n = 2$ (for indirect transition). Direct excitonic transition corresponding to A exciton (~670 nm) and B exciton (~610 nm) could be detected from UV-vis absorption spectra. Moreover, significant amount of indirect band gap contribution was observed for all the nanostructures from the Tauc plot (Fig. 10) having smaller in magnitude in comparison with direct band gap.[65] The average band gap (E_g) values were estimated from the intercept of the linear portion of the $(\alpha h\nu)^2$ and $(\alpha h\nu)^{1/2}$ versus $h\nu$ plots on the $h\nu$ axis (i.e., $(\alpha h\nu)^2 = 0$ and $(\alpha h\nu)^{1/2} = 0$) as shown in Fig. 10. The most interesting results, observed from individual Tauc's plot of undoped MoS_2 and 2%, 4%, 6% Co^{2+} doped MoS_2, is that the E_{gap}, calculated from the absorption spectrum, first decreased and then increased with increasing Co^{2+} doping.

The observations indicate that the incorporation of TM ions lifts the valence band edge causing decrease in band gap which is consistent with theoretical result obtained from DFT calculation.[66] In case of 8% Co doped MoS_2 sample, due to incorporation of heavy amount of dopant ion, defect states appear in conduction band. Consequently, the absorption edge of the conduction band is pushed to the higher energies resulting in widening of band gap to 2.25 eV (blue shift of the excitation peaks) attributing to Moss–Burstein effect[67] (Fig. 9(a)). The variation of band gap (Fig. 9(b)), exciton energies and spin–orbit splitting with various (2%, 4%, 6%, 8%) amount of cobalt doping percentages (A, B excitons) are listed in Table 4.

3.8. Catalytic activity

The catalytic activity of undoped and Co doped MoS_2 nanostructures have been investigated through the reduction of p-nitrophenol (NP) to p-aminophenol (AP) in an excess amount of $NaBH_4$. For the experiment, aqueous stocks of MoS_2 samples, p-

Table 4 Variation of band gap, exciton energies and spin−orbit splitting with doping (A, B excitons)

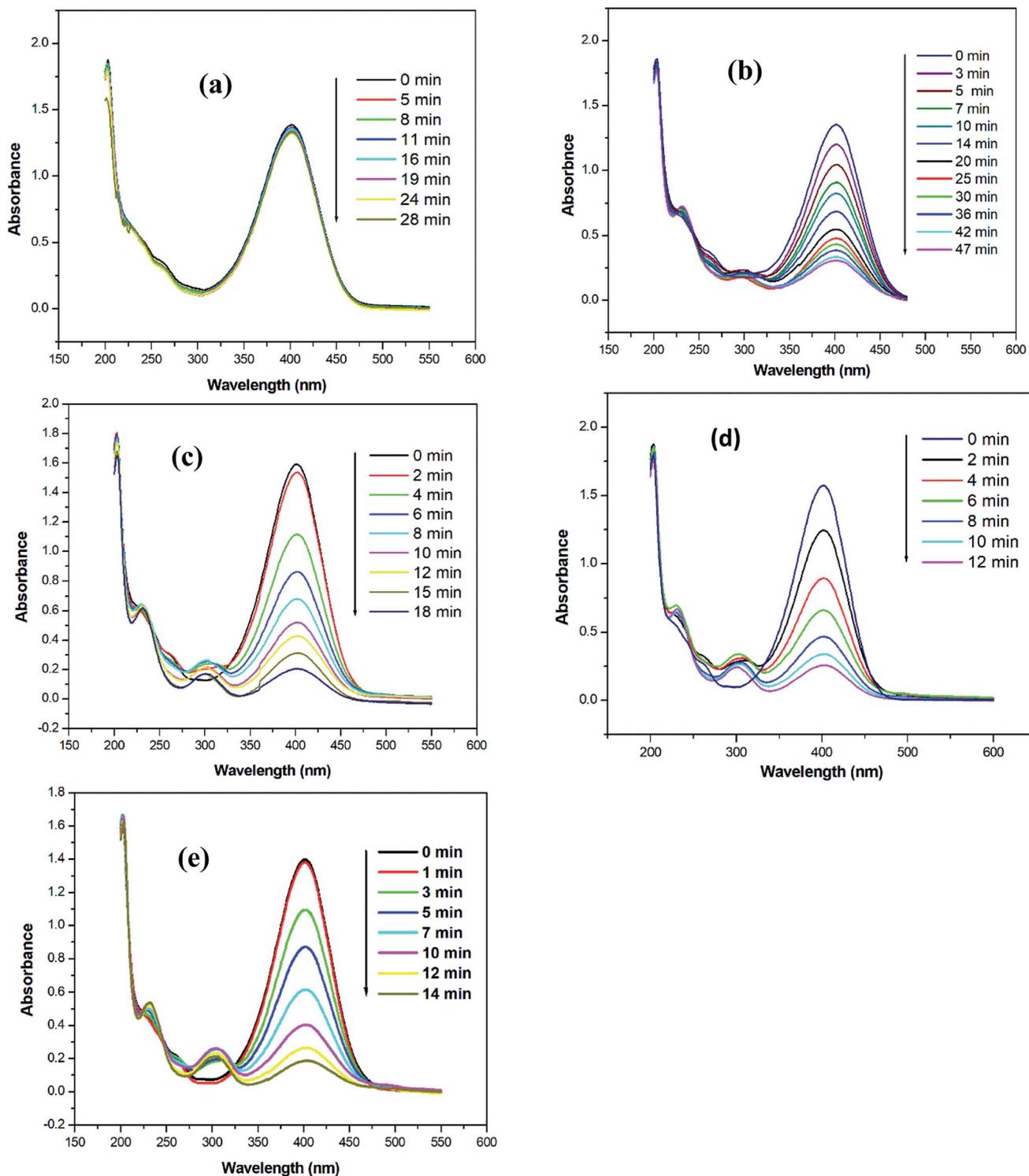| Doping concentration	Direct B. G (eV)	Indirect B. G (eV)	Exciton A (eV)	Exciton B (eV)	Spin–orbit splitting (eV)
0%	2.30	1.60	1.85	2.01	0.16
2%	2.24	1.54	1.83	1.98	0.15
4%	2.11	1.53	1.82	1.96	0.14
6%	2.09	1.52	1.83	1.96	0.13
8%	2.25	1.53	1.84	2.02	0.18

Fig. 11 Time-dependent UV-visible absorption spectra of the reduction of p-NP by excess NaBH$_4$ in the presence of: (a) undoped MoS$_2$; (b) 2% Co doped MoS$_2$; (c) 4% Co doped MoS$_2$; (d) 6% Co doped MoS$_2$; and (e) 8% Co doped MoS$_2$. Condition: [p-NP] = 10^{-2} M, [NaBH$_4$] = 0.1 M, and [Catalyst] = 2 g L^{-1}.

NP, and NaBH$_4$ were prepared at concentrations of 2 g L^{-1}, 10^{-2} (M), and 0.1 (M), respectively. The stock of NaBH$_4$ was maintained at 4 °C to restrain the evolution of H$_2$ gas. Aliquots of 3.0 mL of 0.1 (M) NaBH$_4$, 20 μL of 10^{-2} (M) p-NP, and 5 μL of

MoS$_2$ samples were taken from the respective stocks and mixed together and their absorption spectra were monitored between 450 nm and 600 nm at different time intervals. For control, the study was also carried out in the absence of MoS$_2$. All the graphs
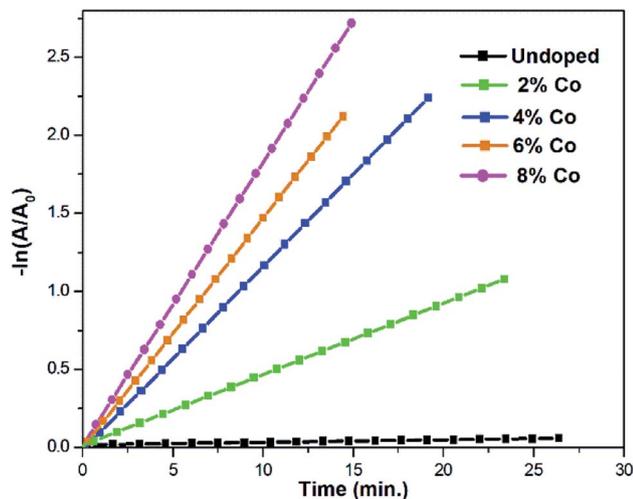
Fig. 12 Plots of $-\ln(A_t/A_0)$ versus time for the reduction of p-NP by NaBH$_4$ in the presence of undoped MoS$_2$, 2% Co, 4% Co, 6% and 8% Co doped MoS$_2$ nanostructures. Conditions: 3.0 mL of 0.1 M NaBH$_4$, 20 µL of 10^{-2} M 4-NP, and 5 µL of 2 g L^{-1} nanocatalysts.

have been plotted based on the average values obtained from three repeat sets of the experiments.

The catalytic efficiency of MoS$_2$ and Co doped MoS$_2$ nanostructures has been evaluated by studying the model reaction of reduction of p-NP by excess NaBH$_4$ using UV-visible spectroscopy.[44] The reduction of p-NP to p-AP by NaBH$_4$ is not a kinetically favourable process due to large difference in the redox potential of the donor and acceptor couple (*i.e.*, $E\{(\text{H}_3\text{BO}_3)(\text{aq.})/(\text{BH}_4^-)(\text{aq.})\} = -1.33$ V and $E\{(p\text{-NP})(\text{aq.})/(p\text{-AP})(\text{aq.})\} = 0.76$ V versus Normal Hydrogen Electrode (NHE), respectively.[68] In the presence of a catalyst, the reaction rate is accelerated by overcoming the kinetic restrictions[69] on the electron transfer from donor BH$_4^-$ to acceptor p-NP. In the present reduction process, the aqueous solution of p-NP ($\lambda = 317$ nm) having light yellow colour was observed to change to deep yellow along with a spectral shift of the absorbance peak to 400 nm. The alkalinity of the solution is increased with the addition of excess of freshly prepared ice-cold aqueous solution of NaBH$_4$ by the formation of the p-nitrophenolate ion in solution. The reduction reaction was manifested by a decrease in absorbance at $\lambda = 400$ nm with fading of the yellow colour of the solution and concurrent appearance of a gradually intensifying new peak at $\lambda = 295$ nm

due to the formation of the reduced product, p-AP [Fig. 11(a)–(e)]. The reduction process of p-NP to p-AP in presence of Co doped MoS$_2$ catalyst and NaBH$_4$ is depicted step by step in Fig. 13. The progress of the reaction with time or the kinetics of the reaction was observed in terms of the concentrations of p-nitrophenolate ions in the reaction mixture by monitoring the changes in absorbance at $\lambda = 400$ nm at different time intervals. The reaction between p-NP and excess NaBH$_4$ has been taken as the control, since the absorbance at $\lambda = 400$ nm was found to remain unaltered with time in the absence of undoped and Co doped MoS$_2$ samples in the reaction mixture. It is noteworthy to mention that the presence of Co doped MoS$_2$ nanostructures did not affect the absorbance spectra of either the p-nitrophenolate ions or p-NP because of their very low concentration[69] ($\sim$3 ppm) in the system. For the studied reduction reaction, the concentration of the reducing agent, NaBH$_4$, has been used in large quantities ($\sim$50 times) with respect to p-NP and catalysts. High concentration, increased pH, and ice-cold condition of the freshly prepared aqueous solution of NaBH$_4$ ensured the stability of the borohydride anion in the reaction medium by dampening its decomposition/protonolysis to liberate hydrogen gas. Small amount of hydrogen gas was released assisted in circumventing the aerial oxidation of p-AP[69] by providing a reducing atmosphere *in situ*. The bubbles of hydrogen gas released during the reaction also helped in stirring the reaction mixture.[68] A large excess of NaBH$_4$ compared with the concentration of p-NP also ensured that the concentration of BH$_4(-)$ ions in the reaction medium remained invariant during the reaction. In addition, occurrence of only one isosbestic point in the UV-visible absorption spectra of the reduction of p-NP (as is evident from Fig. 11) signified that the reaction mixture involved only a pair of species, p-NP and p-AP[70] that varied in concentration and activity of nanocatalysts. From these observations, it may be inferred that the reduction of p-NP followed pseudo-first-order kinetics.[69] Thus, by taking the absorbance of the principal species (*i.e.*, p-nitrophenolate ions) to be proportional to their respective concentrations, the rate constant of the reaction, in the presence of undoped, 2%, 4%, 6%, 8% Co doped MoS$_2$ was determined using the equation

$$-\ln(C_t/C_0) = -\ln(A_t/A_0) = kt$$

where A_t and A_0 are the absorbance (at $\lambda = 400$ nm) at times t and 0, respectively, while C_t and C_0 are the equivalent concentrations of p-nitrophenolate ions at times t and 0, respectively.
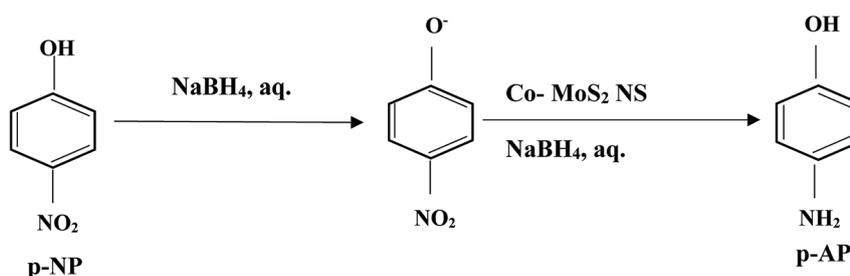

Fig. 13 Diagram of the reduction of p-nitrophenol (p-NP) to p-aminophenol (p-AP) by NaBH$_4$ catalysed by cobalt doped MoS$_2$ NP.

Table 5 Enhancement of rate constant and TOF with increasing cobalt doping in MoS_2

Doping percentages	Rate constant (k; s^{-1})	TOF (molecules per g per s)
0%	2.55×10^{-5}	1.02×10^{17}
2%	5.16×10^{-4}	1.06×10^{18}
4%	1.95×10^{-3}	2.70×10^{18}
6%	3.03×10^{-3}	4.18×10^{18}
8%	2.45×10^{-3}	3.13×10^{18}

The apparent rate constants (k) in the presence of each of the undoped and Co doped MoS_2 nanostructured samples were determined from the slopes of the respective linear plots of $[-\ln(A_t/A_0)]$ versus time, as shown in Fig. 12. The plots shown in Fig. 12 depict the linearity of $[-\ln(A_t/A_0)]$ with time; exponential decay profiles of the absorbance with time support pseudo-first order kinetics with respect to p-nitrophenolate ion. From Fig. 11(d), the 6% Co doped MoS_2 was found to be the most superior catalyst compared to the other. The turnover frequencies (TOF) of the different MoS_2 nanostructures with various cobalt dopant concentrations have been calculated using the expression

$$\text{TOF} = \frac{\text{number of molecules of substrate}}{\text{number of grams of catalyst} \times \text{time in seconds}}$$

where 1×10^{-2} M of p-NP has been taken as the substrate and 2g L^{-1} of the nanostructured MoS_2 as the catalyst. The variation of rate constant and turn over frequency (TOF) with cobalt doping in MoS_2 substrate are listed in Table 5. Table 6 presents the comparison of TOF values of different nanocomposites of MoS_2 reported earlier and our obtained results. The catalytic efficiency of MoS_2 nanostructure is enhanced with the increase of cobalt doping percentages. In Co-doped MoS_2, Co^{2+} takes residence at the coordinative unsaturated sulphur vacancies on the basal plane, edge sites[23,41] substituting Mo atoms. This leads

to a conversion of a fraction of Mo^{4+} to Mo^{3+}, thus stabilizing the 1T polytype.[28] Doped Co^{2+} distorts the close-packed sulphur layer of MoS_2 and induces lattice strain.[71,72] These sites would lower the reaction free energy.[41] Nitrophenol is adsorbed at the strained active sites of the MoS_2 surface.[71–73] At these sites, the electron transfer to the MoS_2 surface is facilitated by Co^{2+}/Co^{3+} redox couple. The electrons generated by the hydrolysis of $NaBH_4$ are transferred to the Co^{2+}-accommodated basal and edge sites of 1T MoS_2 and are promoted into the MoS_2 conduction band.[71] Also, metallic Co^{2+} ions may act as traps for the photo-generated electrons, due to the Schottky barrier created at the metal–semiconductor interface. As a consequence of this trapping phenomenon, the electrons generated in the photocatalytic process and trapped in the metal ions can be transferred to the adsorbed p-NPhate ion on the surface of MoS_2. The electron transfer from the semiconductor to the nitro group of the p-nitrophenolate ion favours the reaction to the formation of the p-AP product. Co substituted sites not only raise faster electron transfer for nitrophenol reduction through reversible reduction–oxidation reactions but also serve as an electron reserve and aid in the retention of the 1T phase with enhanced electrical conductivity. In our study the optimal dopant concentration obtained is 6 at. wt%. since higher concentration (8 at. wt%) of cobalt ion loading possibly leads to partial blockage of catalytic active sites of MoS_2 support surface resulting in enhanced frequency of charge carrier recombination.

4. Conclusion

Undoped and various (2%, 4%, 6% and 8%) atomic weight percentages of cobalt doped MoS_2 nanosheets with the cobalt ion activated on defective basal planes, S-edges, Mo sites are synthesized in a single-step hydrothermal reaction process. The effectiveness of the prepared MoS_2 nanostructures as catalysts for the reduction of 4-nitrophenol to 4-aminophenol in excess $NaBH_4$ has been assessed. All prepared morphologies of MoS_2 nanostructures were found to be effective and stable catalysts and followed pseudo-first-order kinetics. The catalytic activity property was clearly observed to enhance with cobalt doping percentages and also provides far more improved result compared to noble metal and rGO-based MoS_2 nanocomposites reported earlier. Readily dispersible in polar solvents like water or methanol, the 6% Co-doped MoS_2 nanosheets exhibit exceptional catalytic activity toward reduction of harmful nitrophenol from waste waters at ambient temperature exhibiting high turnover frequency (4.18×10^{18} molecules per g per s). Apart from that the observed high negative zeta potential indicates that our reported samples are stable against aggregation in dispersion medium. The superior catalytic activity of the highest 6% Co doped MoS_2 layers is possibly due to a combination of (a) stabilization of the metallic 1T phase with increasing electrical conductivity (decreasing band gap and activation energy) and (b) better electron capture from the hydride and electron supply to the nitrophenol substrates through reversible redox reactions at the Co sites. In a nutshell, our study clearly exhibits that proper tuning of Co doping in

Table 6 Comparison of the TOF values for the catalytic reduction of p-NP

Catalyst sample	TOF (min^{-1})	Reference
2H-chemically exfoliated MoS_2	1.5×10^{-2}	(Guardia et al. 2014)[74]
MoS_2–rGO	1.50×10^{-1}	(Anto Jeffery et al. 2017)[75]
MoS_2–Pd	3.20×10^{-3}	(Qiao et al. 2017)[76]
MoS_2–Fe_3O_4	4.00×10^{-2}	(Lin et al. 2015)[77]
MoS_2–Fe_3O_4/Pt	6.00×10^{-4}	(Cheng et al. 2015)[78]
MoS_2	5.11×10^{-3}	(Qiao et al. 2018)[79]
MoS_2	2.50×10^{-3}	This work
2% Co doped MoS_2	3.10×10^{-2}	This work
4% Co doped MoS_2	1.17×10^{-1}	This work
6%Co doped MoS_2	1.82×10^{-1}	This work
8% Co doped MoS_2	1.47×10^{-1}	This work
Ni–Co alloy	4.63×10^{-3}	(Wu et al. 2011)[80]
Au–Fe_3O_4 NPs	2.80×10^{-3}	(Lin et al. 2011)[81]
Pd–Fe_3O_4@SiO_2	1.95×10^{-2}	(Wang et al. 2014)[82]
AgNPs	2.09×10^{-3}	(Liang et al. 2013)[83]

MoS_2 nanosheets is another potential alternative of noble metal catalyst for the catalytic reduction of nitroarene.

Conflicts of interest

There are no conflicts to declare.

Acknowledgements

References

1 M. Chhowalla, H. S. Shin, G. Eda, L. Li, K. P. Loh and H. Zhang, The chemistry of two-dimensional layered transition metal dichalcogenide nanosheets, *Nat. Chem.*, 2013, **5**, 263–275.

2 B. Hinnemann, P. G. Moses, J. Bonde, K. P. Jørgensen, J. H. Nielsen, S. Horch, I. Chorkendorff and J. K. Nørskov, Biomimetic hydrogen evolution: MoS2 nanoparticles as catalyst for hydrogen evolution, *J. Am. Chem. Soc.*, 2005, **127**, 5308–5309.

3 X. Chia, A. Y. S. Eng, A. Ambrosi, S. M. Tan and M. Pumera, Electrochemistry of Nanostructured Layered Transition-Metal Dichalcogenides, *Chem. Rev.*, 2015, **115**, 11941–11966.

4 T. F. Jaramillo, K. P. Jorgensen, J. Bonde, J. H. Nielsen, S. Horch and I. Chorkendorff, Identification of Active Edge Sites for Electrochemical H2 Evolution from MoS2 Nanocatalysts, *Science*, 2007, **317**, 100–102.

5 G. A. Somorjai and V. H. J. De Beer, Structure and Function of The Catalyst and The Promoter In Co—Mo Hydrodesuifurization Catalysts, *Catal. Rev.*, 1989, **31**, 1–41.

6 P. Clark, W. Li and S. T. Oyama, Synthesis and activity of a new catalyst for hydroprocessing: Tungsten phosphide, *J. Catal.*, 2001, **200**, 140–147.

7 C. Ataca, H. Şahin, E. Aktuörk and S. Ciraci, Mechanical and electronic properties of MoS2 nanoribbons and their defects, *J. Phys. Chem. C*, 2011, **115**, 3934–3941.

8 J. Heising and M. G. Kanatzidis, Structure of restacked MoS2 and WS2 elucidated by electron crystallography, *J. Am. Chem. Soc.*, 1999, **121**, 638–643.

9 F. Wypych and R. Schöllhorn, 1T-MoS2, a new metallic modification of molybdenum disulfide, *J. Chem. Soc., Chem. Commun.*, 1992, 1386–1388.

10 B. Radisavljevic, A. Radenovic, J. Brivio, V. Giacometti and A. Kis, Single-layer MoS2 transistors, *Nat. Nanotechnol.*, 2011, **6**, 147–150.

11 K. Zhang, S. Feng, J. Wang, A. Azcatl, N. Lu, R. Addou, N. Wang, C. Zhou, J. Lerach, V. Bojan, M. J. Kim, L. Q. Chen, R. M. Wallace, M. Terrones, J. Zhu and J. A. Robinson, Manganese Doping of Monolayer MoS 2: The Substrate Is Critical, *Nano Lett.*, 2015, **15**, 6586–6591.

12 J. Shakya, S. Kumar, D. Kanjilal and T. Mohanty, Work Function Modulation of Molybdenum Disulfide Nanosheets by Introducing Systematic Lattice Strain, *Sci. Rep.*, 2017, **7**, 9576.

13 J. Li, C. Y. Liu and Y. Liu, Au/graphene hydrogel: Synthesis, characterization and its use for catalytic reduction of 4-nitrophenol, *J. Mater. Chem.*, 2012, **22**, 8426–8430.

14 Y. Li, Y. Cao, J. Xie, D. Jia, H. Qin and Z. Liang, Facile solid-state synthesis of Ag/graphene oxide nanocomposites as highly active and stable catalyst for the reduction of 4-nitrophenol, *Catal. Commun.*, 2015, **58**, 21–25.

15 J. J. Lv, A. J. Wang, X. Ma, R. Y. Xiang, J. R. Chen and J. J. Feng, One-pot synthesis of porous Pt-Au nanodendrites supported on reduced graphene oxide nanosheets toward catalytic reduction of 4-nitrophenol, *J. Mater. Chem. A*, 2015, **3**, 290–296.

16 X. Chen, X. Chen, Z. Cai and M. Oyama, AuPd bimetallic nanoparticles decorated on graphene nanosheets: Their green synthesis, growth mechanism and high catalytic ability in 4-nitrophenol reduction, *J. Mater. Chem. A*, 2014, **2**, 5668–5674.

17 K. Layek, M. L. Kantam, M. Shirai, D. Nishio-Hamane, T. Sasaki and H. Maheswaran, Gold nanoparticles stabilized on nanocrystalline magnesium oxide as an active catalyst for reduction of nitroarenes in aqueous medium at room temperature, *Green Chem.*, 2012, **14**, 3164–3174.

18 J. Lee, J. C. Park and H. Song, A Nanoreactor framework of a Au@SiO2 yolk/shell structure for catalytic reduction of p-nitrophenol, *Adv. Mater.*, 2008, **20**, 1523–1528.

19 Y. Li, Q. Chen, Z. Zhang, Q. Li and X. Qiao, Effects of morphology and crystallinity of MoS2 nanocrystals on the catalytic reduction of p-nitrophenol, *J. Nanoparticle Res.*, 2018, **20**, 327.

20 J. D. Benck, Z. Chen, L. Y. Kuritzky, A. J. Forman and T. F. Jaramillo, Amorphous molybdenum sulfide catalysts for electrochemical hydrogen production: Insights into the origin of their catalytic activity, *ACS Catal.*, 2012, **2**, 1916–1923.

21 D. Merki and X. Hu, Recent developments of molybdenum and tungsten sulfides as hydrogen evolution catalysts, *Energy Environ. Sci.*, 2011, **4**, 3878.

22 C. G. Morales-Guio and X. Hu, Amorphous molybdenum sulfides as hydrogen evolution catalysts, *Acc. Chem. Res.*, 2014, **47**, 2671–2681.

23 J. Bonde, P. G. Moses, T. F. Jaramillo, J. K. Nørskov and I. Chorkendorff, Hydrogen evolution on nano-particulate transition metal sulfides, *Faraday Discuss.*, 2008, **140**, 219–231.

24 J. Kibsgaard, Z. Chen, B. N. Reinecke and T. F. Jaramillo, Engineering the surface structure of MoS2 to Â preferentially expose active edge sites forÂ electrocatalysis, *Nat. Mater.*, 2012, **11**, 963–969.

25 J. Xie, H. Zhang, S. Li, R. Wang, X. Sun, M. Zhou, J. Zhou, X. W. Lou and Y. Xie, Defect-rich MoS2 ultrathin nanosheets with additional active edge sites for enhanced electrocatalytic hydrogen evolution, *Adv. Mater.*, 2013, **25**, 5807–5813.

26 J. Xie, J. Zhang, S. Li, F. Grote, X. Zhang, H. Zhang, R. Wang, Y. Lei, B. Pan and Y. Xie, Controllable disorder engineering in oxygen-incorporated MoS2 ultrathin nanosheets for efficient hydrogen evolution, *J. Am. Chem. Soc.*, 2013, **135**, 17881–17888.

27 D. Kong, H. Wang, J. J. Cha, M. Pasta, K. J. Koski, J. Yao and Y. Cui, Synthesis of MoS2 and MoSe2 films with vertically aligned layers, *Nano Lett.*, 2013, **13**, 1341–1347.

28 H. Wang, Z. Lu, S. Xu, D. Kong, J. J. Cha, G. Zheng, P. C. Hsu, K. Yan, D. Bradshaw, F. B. Prinz and Y. Cui, Electrochemical tuning of vertically aligned MoS2 nanofilms and its application in improving hydrogen evolution reaction, *Proc. Natl. Acad. Sci. U. S. A.*, 2013, **110**, 19701–19706.

29 Y. Li, H. Wang, L. Xie, Y. Liang, G. Hong and H. Dai, MoS2 nanoparticles grown on graphene: An advanced catalyst for the hydrogen evolution reaction, *J. Am. Chem. Soc.*, 2011, **133**, 7296–7299.

30 H. Wang, Z. Lu, D. Kong, J. Sun, T. M. Hymel and Y. Cui, Electrochemical tuning of MoS2 nanoparticles on three-dimensional substrate for efficient hydrogen evolution, *ACS Nano*, 2014, **8**, 4940–4947.

31 A. A. Jeffery, S. R. Rao and M. Rajamathi, Preparation of MoS2–reduced graphene oxide (rGO) hybrid paper for catalytic applications by simple exfoliation–costacking, *Carbon*, 2017, **112**, 8–16.

32 F. Z. Wang, M. J. Zheng, B. Zhang, C. Q. Zhu, Q. Li, L. Ma and W. Z. Shen, Ammonia intercalated flower-like MoS2 nanosheet film as electrocatalyst for high efficient and stable hydrogen evolution, *Sci. Rep.*, 2016, **6**, 31092.

33 M.-R. Gao, J.-X. Liang, Y.-R. Zheng, Y.-F. Xu, J. Jiang, Q. Gao, J. Li and S.-H. Yu, An efficient molybdenum disulfide/cobalt diselenide hybrid catalyst for electrochemical hydrogen generation, *Nat. Commun.*, 2015, **6**, 5982.

34 J. Huang, D. Hou, Y. Zhou, W. Zhou, G. Li, Z. Tang, L. Li and S. Chen, MoS2 nanosheet-coated CoS2 nanowire arrays on carbon cloth as three-dimensional electrodes for efficient electrocatalytic hydrogen evolution, *J. Mater. Chem. A*, 2015, **3**, 22886–22891.

35 R. Bose, Z. Jin, S. Shin, S. Kim, S. Lee and Y. S. Min, Co-catalytic Effects of CoS2 on the Activity of the MoS2 Catalyst for Electrochemical Hydrogen Evolution, *Langmuir*, 2017, **33**, 5628–5635.

36 W. Wang, L. Li, K. Wu, G. Zhu, S. Tan, Y. Liu and Y. Yang, Highly selective catalytic conversion of phenols to aromatic hydrocarbons on CoS2/MoS2 synthesized using a two step hydrothermal method, *RSC Adv.*, 2016, **6**, 31265–31271.

37 I. Sorribes, L. Liu and A. Corma, Nanolayered Co-Mo-S Catalysts for the Chemoselective Hydrogenation of Nitroarenes, *ACS Catal.*, 2017, **7**, 2698–2708.

38 X. L. Yin, L. L. Li, W. J. Jiang, Y. Zhang, X. Zhang, L. J. Wan and J. S. Hu, MoS2/CdS Nanosheets-on-Nanorod Heterostructure for Highly Efficient Photocatalytic H2 Generation under Visible Light Irradiation, *ACS Appl. Mater. Interfaces*, 2016, **8**, 15258–15266.

39 Y. Liu, Y. X. Yu and W. De Zhang, MoS2/CdS heterojunction with high photoelectrochemical activity for H2 evolution under visible light: The role of MoS2, *J. Phys. Chem. C*, 2013, **117**, 12949–12957.

40 T. Lin, J. Wang, L. Guo and F. Fu, Fe3O4@MoS2 core-shell composites: Preparation, characterization, and catalytic application, *J. Phys. Chem. C*, 2015, **119**, 13658–13664.

41 D. Voiry, H. Yamaguchi, J. Li, R. Silva, D. C. B. Alves, T. Fujita, M. Chen, T. Asefa, V. B. Shenoy, G. Eda and M. Chhowalla, Enhanced catalytic activity in strained chemically exfoliated WS 2 nanosheets for hydrogen evolution, *Nat. Mater.*, 2013, **12**, 850–855.

42 M. A. Lukowski, A. S. Daniel, F. Meng, A. Forticaux, L. Li and S. Jin, Enhanced hydrogen evolution catalysis from chemically exfoliated metallic MoS2 nanosheets, *J. Am. Chem. Soc.*, 2013, **135**, 10274–10277.

43 Y. Wang, B. J. Carey, W. Zhang, A. F. Chrimes, L. Chen, K. Kalantar-Zadeh, J. Z. Ou and T. Daeneke, Intercalated 2D MoS2 Utilizing a Simulated Sun Assisted Process: Reducing the HER Overpotential, *J. Phys. Chem. C*, 2016, **120**, 2447–2455.

44 X. Q. Qiao, Z. W. Zhang, F. Y. Tian, D. F. Hou, Z. F. Tian, D. S. Li and Q. Zhang, Enhanced Catalytic Reduction of p-Nitrophenol on Ultrathin MoS2 Nanosheets Decorated with Noble Metal Nanoparticles, *Cryst. Growth Des.*, 2017, **17**, 3538–3547.

45 Y. Yan, B. Xia, Z. Xu and X. Wang, Recent Development of Molybdenum Sulfides as Advanced Electrocatalysts for Hydrogen Evolution Reaction, *ACS Catal.*, 2014, **4**, 1693–1705.

46 D. Merki, H. Vrubel, L. Rovelli, S. Fierro and X. Hu, Fe, Co, and Ni ions promote the catalytic activity of amorphous molybdenum sulfide films for hydrogen evolution, *Chem. Sci.*, 2012, **3**, 2515–2525.

47 H. Wang, H. Yuan, S. Sae Hong, Y. Li and Y. Cui, Physical and chemical tuning of two-dimensional transition metal dichalcogenides, *Chem. Soc. Rev.*, 2015, **44**, 2664–2680.

48 C. Nethravathi, J. Prabhu, S. Lakshmipriya and M. Rajamathi, Magnetic Co-Doped MoS 2 Nanosheets for Efficient Catalysis of Nitroarene Reduction, *ACS Omega*, 2017, **2**, 5891–5897.

49 G. Liu, A. W. Robertson, M. M. J. Li, W. C. H. Kuo, M. T. Darby, M. H. Muhieddine, Y. C. Lin, K. Suenaga, M. Stamatakis, J. H. Warner and S. C. E. Tsang, MoS2 monolayer catalyst doped with isolated Co atoms for the hydrodeoxygenation reaction, *Nat. Chem.*, 2017, **9**, 810–816.

50 A. Azcatl, X. Qin, A. Prakash, C. Zhang, L. Cheng, Q. Wang, N. Lu, M. J. Kim, J. Kim, K. Cho, R. Addou, C. L. Hinkle, J. Appenzeller and R. M. Wallace, Covalent Nitrogen Doping and Compressive Strain in MoS2 by Remote N2 Plasma Exposure, *Nano Lett.*, 2016, **16**, 5437–5443.

51 J. Wang, F. Sun, S. Yang, Y. Li, C. Zhao, M. Xu, Y. Zhang and H. Zeng, Robust ferromagnetism in Mn-doped MoS 2 nanostructures, *Appl. Phys. Lett.*, 2016, **109**, 092401.

52 S. Pak, J. Lee, Y. W. Lee, A. R. Jang, S. Ahn, K. Y. Ma, Y. Cho, J. Hong, S. Lee, H. Y. Jeong, H. Im, H. S. Shin, S. M. Morris, S. Cha, J. I. Sohn and J. M. Kim, Strain-Mediated Interlayer Coupling Effects on the Excitonic Behaviors in an

Epitaxially Grown MoS2/WS2 van der Waals Heterobilayer, *Nano Lett.*, 2017, **17**, 5634–5640.

53 X. Dai, K. Du, Z. Li, M. Liu, Y. Ma, H. Sun, X. Zhang and Y. Yang, Co-Doped MoS2 Nanosheets with the Dominant CoMoS Phase Coated on Carbon as an Excellent Electrocatalyst for Hydrogen Evolution, *ACS Appl. Mater. Interfaces*, 2015, **7**, 27242–27253.

54 H. Li, Q. Zhang, C. C. R. Yap, B. K. Tay, T. H. T. Edwin, A. Olivier and D. Baillargeat, From bulk to monolayer MoS 2: Evolution of Raman scattering, *Adv. Funct. Mater.*, 2012, **22**, 1385–1390.

55 M. R. Gao, M. K. Y. Chan and Y. Sun, Edge-terminated molybdenum disulfide with a 9.4-Å interlayer spacing for electrochemical hydrogen production, *Nat. Commun.*, 2015, **6**, 1–8.

56 A. El Mragui, Y. Logvina, L. Pinto da Silva, O. Zegaoui and J. C. G. Esteves da Silva, Synthesis of Fe- and Co-Doped TiO2 with Improved Photocatalytic Activity Under Visible Irradiation Toward Carbamazepine Degradation, *Materials*, 2019, **12**, 3874.

57 K. Das, S. N. Sharma, M. Kumar and S. K. De, Morphology dependent luminescence properties of Co doped TiO2 nanostructures, *J. Phys. Chem. C*, 2009, **113**, 14783–14792.

58 N. Thi Xuyen and J.-M. Ting, Hybridized 1T/2H MoS 2 Having Controlled 1T Concentrations and its use in Supercapacitors, *Chem. - Eur. J.*, 2017, **23**, 17348–17355.

59 S. Eijsbouts, J. J. L. Heinerman and H. J. W. Elzerman, MoS2 structures in high-activity hydrotreating catalysts. I. Semi-quantitative method for evaluation of transmission electron microscopy results. Correlations between hydrodesulfurization and hydrodenitrogenation activities and MoS2 dispersion, *Appl. Catal., A*, 1993, **105**, 53–68.

60 M. S. Faber, R. Dziedzic, M. A. Lukowski, N. S. Kaiser, Q. Ding and S. Jin, High-performance electrocatalysis using metallic cobalt pyrite (CoS 2) micro- and nanostructures, *J. Am. Chem. Soc.*, 2014, **136**, 10053–10061.

61 M. Cabán-Acevedo, M. L. Stone, J. R. Schmidt, J. G. Thomas, Q. Ding, H. C. Chang, M. L. Tsai, H. He and S. Jin, Efficient hydrogen evolution catalysis using ternary pyrite-type cobalt phosphosulphide, *Nat. Mater.*, 2015, **14**, 1245–1251.

62 D. C. Higgins, F. M. Hassan, M. H. Seo, J. Y. Choi, M. A. Hoque, D. U. Lee and Z. Chen, Shape-controlled octahedral cobalt disulfide nanoparticles supported on nitrogen and sulfur-doped graphene/carbon nanotube composites for oxygen reduction in acidic electrolyte, *J. Mater. Chem. A*, 2015, **3**, 6340–6350.

63 G. Zhang, W. Lu, F. Cao, Z. Xiao and X. Zheng, N-doped graphene coupled with Co nanoparticles as an efficient electrocatalyst for oxygen reduction in alkaline media, *J. Power Sources*, 2016, **302**, 114–125.

64 N. Dong, Y. Li, Y. Feng, S. Zhang, X. Zhang, C. Chang, J. Fan, L. Zhang and J. Wang, Optical Limiting and Theoretical Modelling of Layered Transition Metal Dichalcogenide Nanosheets, *Sci. Rep.*, 2015, **5**, 14646.

65 N. Saha, A. Sarkar, A. B. Ghosh, A. K. Dutta, G. R. Bhadu, P. Paul and B. Adhikary, Highly active spherical amorphous MoS2: Facile synthesis and application in photocatalytic degradation of rose bengal dye and hydrogenation of nitroarenes, *RSC Adv.*, 2015, **5**, 88848–88856.

66 A. Ramasubramaniam and D. Naveh, Mn-doped monolayer MoS2: An atomically thin dilute magnetic semiconductor, *Phys. Rev. B: Condens. Matter Mater. Phys.*, 2013, **87**, 1–7.

67 Q. C. Sun, L. Yadgarov, R. Rosentsveig, G. Seifert, R. Tenne and J. L. Musfeldt, Observation of a Burstein–Moss Shift in Rhenium-Doped MoS 2 Nanoparticles, *ACS Nano*, 2013, **7**, 3506–3511.

68 S. Saha, A. Pal, S. Kundu, S. Basu and T. Pal, Photochemical green synthesis of calcium-alginate-stabilized ag and au nanoparticles and their catalytic application to 4-nitrophenol reduction, *Langmuir*, 2010, **26**, 2885–2893.

69 A. Gangula, R. Podila, R. M. L. Karanam, C. Janardhana and A. M. Rao, Catalytic reduction of 4-nitrophenol using biogenic gold and silver nanoparticles derived from breynia rhamnoides, *Langmuir*, 2011, **27**, 15268–15274.

70 G. Q. Gao, L. Lin, C. M. Fan, Q. Zhu, R. X. Wang and A. W. Xu, Highly dispersed platinum nanoparticles generated in viologen micelles with high catalytic activity and stability, *J. Mater. Chem. A*, 2013, **1**, 12206–12212.

71 J. Brenner, C. L. Marshall, L. Ellis, N. Tomczyk, J. Heising and M. Kanatzidis, Microstructural Characterization of Highly HDS-Active Co6S8-Pillared Molybdenum Sulfides, *Chem. Mater.*, 1998, **10**, 1244–1257.

72 R. R. Chianelli, A. F. Ruppert, M. José-Yacamán and A. Vázquez-Zavala, HREM studies of layered transition metal sulfide catalytic materials, *Catal. Today*, 1995, **23**, 269–281.

73 H. Li, S. Chen, X. Jia, B. Xu, H. Lin, H. Yang, L. Song and X. Wang, Amorphous nickel-cobalt complexes hybridized with 1T-phase molybdenum disulfide via hydrazine-induced phase transformation for water splitting, *Nat. Commun.*, 2017, **8**, 15377.

74 L. Guardia, J. I. Paredes, J. M. Munuera, S. Villar-Rodil, M. Ayan-Varela, A. Martinez-Alonso and J. M. D. Tascon, Chemically Exfoliated MoS$_2$ Nanosheets as an Efficient Catalyst for Reduction Reactions in the Aqueous Phase, *ACS Appl. Mater. Interfaces*, 2014, **6**, 21702–21710.

75 A. A. Jeffery, S. R. Rao and M. Rajamathi, Preparation of MoS$_2$–reduced graphene oxide (rGO) hybrid paper for catalytic applications by simple exfoliation–costacking, *Carbon*, 2017, **112**, 8–16.

76 X. Q. Qiao, Z. W Zhang, F. Y. Tian, D. F Hou, Z. F. Tian, D. S Li and Q. Zhang, Enhanced Catalytic Reduction of *p*-Nitrophenol on Ultrathin MoS$_2$ Nanosheets Decorated with Noble Metal Nanoparticles, *Cryst. Growth Des.*, 2017, **17**, 3538–3547.

77 T. Lin, J. Wang, L. Guo and F. Fu, Fe$_3$O$_4$@MoS$_2$ Core–Shell Composites: Preparation, Characterization, and Catalytic Application, *J. Phys. Chem. C*, 2015, **119**, 13658–13664.

78 Z. Cheng, B. He and L. Zhou, A general one-step approach for in situ decoration of MoS$_2$ nanosheets with inorganic nanoparticles, *J. Mater. Chem. A*, 2015, **3**, 1042–1048.

79 X. Q. Qiao, Z. W. Zhang, D. F. Hou, D. S. Li, Y. Liu, Y. Q. Lan, J. Zhang, P. Feng and X. Bu, Tunable MoS$_2$/SnO$_2$ P–N

Heterojunctions for an Efficient Trimethylamine Gas Sensor and 4-Nitrophenol Reduction Catalyst, *ACS Sustainable Chem. Eng.*, 2018, **6**, 12375–12384.

80 C. Wu, Y. Bai, D. X. Liu, F. Wu, M. L. Pang and B. L. Yi, Ni–Co–B catalyst-promoted hydrogen generation by hydrolyzing $NaBH_4$ solution for in situ hydrogen supply of portable fuel cells, *Catalysis Today*, 2011, **170**, 33–39.

81 F. Lin and R. Doong, Bifunctional Au–Fe_3O_4 Heterostructures for Magnetically Recyclable Catalysis of Nitrophenol Reduction, *J. Phys. Chem. C*, 2011, **115**, 6591–6598.

82 P. Wang, H. Liu, J. Niu, R. Li and J. Ma, Entangled Pd complexes over Fe_3O_4@SiO_2 as supported catalysts for hydrogenation and Suzuki reactions, *Catal. Sci. Technol.*, 2014, **4**, 1333–1339.

83 M. Liang, L. Wang, R. Su, W. Qi, M. Wang, Y. Yu and Z. He, Synthesis of silver nanoparticles within cross-linked lysozyme crystals as recyclable catalysts for 4-nitrophenol reduction, *Catal. Sci. Technol.*, 2013, **3**, 1910–1914.